Interdecadal Variation of Precipitation over the Hengduan Mountains during Rainy Seasons

DANHONG DONG,[a,b,c] WEICHEN TAO,[a,b] WILLIAM K. M. LAU,[b,d] ZHANQING LI,[b,d,e] GANG HUANG,[a,c,f,g] AND PENGFEI WANG[a,h]

[a] *State Key Laboratory of Numerical Modeling for Atmospheric Sciences and Geophysical Fluid Dynamics, Institute of Atmospheric Physics, Chinese Academy of Sciences, Beijing, China*
[b] *Earth System Science Interdisciplinary Center, University of Maryland, College Park, College Park, Maryland*
[c] *University of Chinese Academy of Sciences, Beijing, China*
[d] *Department of Atmospheric and Oceanic Science, University of Maryland, College Park, College Park, Maryland*
[e] *State Key Laboratory of Remote Sensing Science, College of Global Change and Earth System Science, Beijing Normal University, Beijing, China*
[f] *Laboratory for Regional Oceanography and Numerical Modeling, Qingdao National Laboratory for Marine Science and Technology, Qingdao, China*
[g] *Joint Center for Global Change Studies, Beijing, China*
[h] *Center for Monsoon System Research, Institute of Atmospheric Physics, Chinese Academy of Sciences, Beijing, China*

(Manuscript received 8 October 2018, in final form 20 February 2019)

ABSTRACT

The present study investigates the interdecadal variation of precipitation over the Hengduan Mountains (HM) during rainy seasons from various reanalysis and observational datasets. Based on a moving *t* test and Lepage test, an obvious rainfall decrease is identified around 2004/05. The spatial distribution of the rainfall changes exhibits large and significant precipitation deficits over the southern HM, with notable anomalous lower-level easterly divergent winds along the southern foothills of the Himalayas (SFH). The anomalous easterlies are located at the northern edge of two cyclones, with two centers of positive rainfall anomalies over the west coast of India (WCI) and the Bay of Bengal (BOB). Observational evidence and numerical experiments demonstrate that the decadal changes of SST over the WP and WIO suppress rainfall over the eastern Indian Ocean (EIO) through large-scale circulation adjustment. The EIO dry anomalies trigger the cross-equatorial anticyclonic wind anomalies as a Rossby wave response, and further cause anomalous meridional circulation and moisture transport over the WCI and BOB, favoring the rainfall increase there. The anomalous easterlies at the northern edge of two cyclones induced by the wet anomalies–related heating cause the divergence anomalies along the SFH, resulting in the reduction of precipitation in the HM. In turn, the two anomalous cyclones and dry anomalies have positive feedback on the wet and easterly wind anomalies, respectively, emphasizing the importance of the circulation–heating interaction.

1. Introduction

The Hengduan Mountains (HM) lie on the southeast side of the Tibetan Plateau (TP) and west side of Sichuan basin, with the YunGui plateau and Bayan Har Mountains on the south and north sides, respectively (Li et al. 2011; K. Zhang et al. 2014; Fang et al. 2017; Dai et al. 2018; Dong et al. 2018). Spanning an area of 500 000 km^2, the HM feature the world's steepest elevation drop from about 4800 to 600 m, within a distance of 500 km from the TP to the Sichuan basin (Fig. 1a). Mountains and rivers alternate there, forming the unique three-dimensional landscape featured with high mountains and deep valleys. Several major rivers in China originate from or flow through this region, including the Yangtze River, the Yellow River, the Lancang River, and the Nu River. The last two are connected downstream to the Mekong River and Salween River over the Indochina Peninsula. Furthermore, the HM are one of the world's most

Supplemental information related to this paper is available at the Journals Online website: https://doi.org/10.1175/JCLI-D-18-0670.s1.

Corresponding author: Weichen Tao, tao@mail.iap.ac.cn

DOI: 10.1175/JCLI-D-18-0670.1

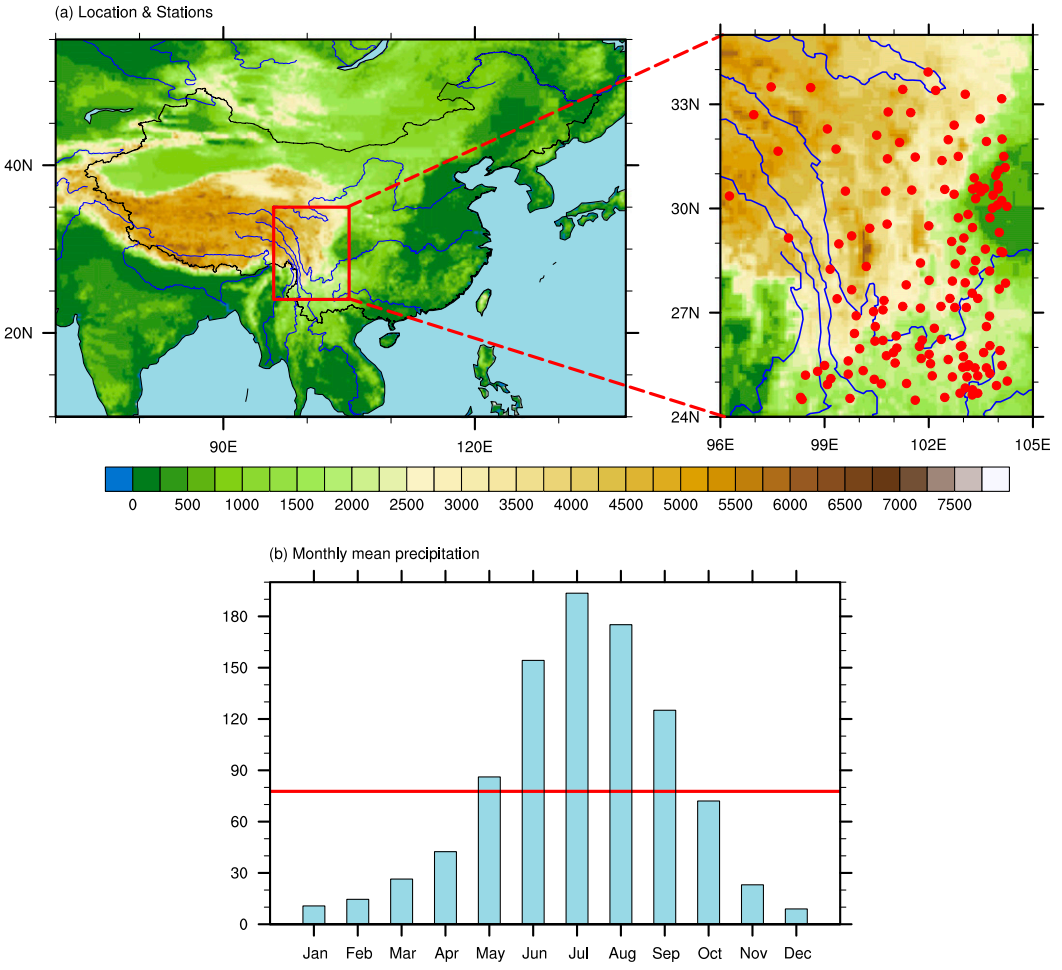

FIG. 1. (a) Geographic location of the HM (red box) and distribution of 151 stations. (b) Climatological monthly mean precipitation (mm) averaged over the HM from 151 station observations for the period of 1979–2014. The red line represents the annual mean.

important biodiversity regions and have more than 9000 species of plants (e.g., Nie et al. 2002; Xing and Ree 2017; Cheng et al. 2018), flourishing in a diverse ecosystem consisting of rivers, lakes, forests, grasslands, and glaciers. Precipitation over the HM is important to the formation of glaciers, the supply of freshwater from surface runoffs, and river discharge (Dong et al. 2016), and thus it has a great impact on the ecological environment and social economy in both local and remote downstream areas.

The HM possess a monsoon climate with prevailing lower-level southwest winds, connecting the South Asian and East Asian summer monsoons (Fig. 7b of Dong et al. 2018), which contribute to the complex and changeable climate in this area (Zhu et al. 2013; P. Zhang et al. 2014). Zhang et al. (2015) found a positive correlation between the rainfall anomalies of the HM and the East Asian summer monsoon. Zhu et al. (2016) indicated that the drought in the HM is mainly due to the unstable rainfall time of the South Asian monsoon. Recently, Dong et al. (2018) found that the interannual variability of precipitation over the HM during rainy seasons is influenced by the combined effect of central and eastern Pacific SST anomalies and the Silk Road pattern (SRP; Lu et al. 2002; Enomoto et al. 2003; Kosaka et al. 2009; Hong and Lu 2016; Gong et al. 2018). These two factors reflect the different aspects of large-scale circulation anomalies affecting HM precipitation. The central and eastern Pacific cooling plays a dominant role in the development of anomalous lower-level cyclone over the South China Sea, which helps moisture convergence over the HM, while the SRP mainly contributes to the anomalous ascending motions there.

Interdecadal variability is an important topic in climate studies. During recent years, substantial attention

has been devoted to the interdecadal changes of precipitation in China, which show strong regional and seasonal features, and the changepoints in different regions and seasons are not same. For example, interdecadal shifts of summer precipitation for the past 60 years in eastern China mainly occurred in the middle and late 1970s, the early 1990s, and the late 1990s (e.g., Ding et al. 2008; Si et al. 2009; Zhou et al. 2009; Liu et al. 2011; Huang et al. 2013; Xu et al. 2015; Ren et al. 2017). The autumn precipitation in southwestern China experienced a notable wet-to-dry shift in 1994 (Wang et al. 2018), whereas an interdecadal shift around the 1980s was detected in western China (Ting et al. 2018). Notable increases and decreases of southern China summer rainfall have been observed after 1993 and 2003, respectively (Ding et al. 2008; Yao et al. 2008; Wu et al. 2010; Xu et al. 2015). At present, the long-term variation of precipitation over the HM is still unclear.

The interdecadal variations of precipitation usually concur with large-scale circulation adjustment, and the sources of the interdecadal changes are complex and not well understood. The roles of SST changes in the tropics and subtropics on precipitation in China have been investigated to a great extent, such as in the tropical oceans (Hu 1997; Weng et al. 1999; Gong and Ho 2002; Li et al. 2010; Wu et al. 2010; Chen et al. 2014; Xu et al. 2015; Ting et al. 2018; Wang et al. 2018) and with reference to the Pacific decadal oscillation (PDO; Ma 2007; Chen et al. 2014; Qian and Zhou 2014; Xu et al. 2015; Yu et al. 2015; Si and Ding 2016; Yang et al. 2017) and the Atlantic multidecadal oscillation (AMO; Qian et al. 2014; Si and Ding 2016; Yang et al. 2017). Additionally, interdecadal changes of precipitation in China could be affected by atmospheric processes at middle and high latitudes via wave train–like teleconnection patterns, such as the SRP (Xu et al. 2015; Hong et al. 2017; Piao et al. 2017; Wang et al. 2017), the North Atlantic Oscillation (Sun et al. 2009; Chen et al. 2017; Hua et al. 2017; Piao et al. 2018), and the Eurasian pattern (Xu et al. 2015). Besides, the local circulation–heating interaction may enhance the signal induced by remote forcing (Xie et al. 2009; Wu et al. 2010; Jiang and Ting 2017; Tao et al. 2017). Henceforth, the present study inspects the long-term variation of precipitation over the HM in recent decades, and aims to acquire better understanding the possible driving factors in both remote and local areas.

The organization of the text is as follows: The data and methods used are described in section 2. Section 3 performs statistical diagnoses and numerical experiments to investigate the interdecadal variation of precipitation over the HM and its connection to atmospheric circulation and SST anomalies. Section 4 provides a further discussion about the plausible role of SRP. A concluding summary is presented in section 5.

2. Data and methods

a. Data

The observed daily precipitation data used in this study are from the National Climatic Center of the China Meteorological Administration with 2472 high-density national meteorological stations. The HM region is defined by a rectangular domain of 24°40′–34°00′N and 96°20′–104°30′E (Fig. 1a), and 151 stations in the HM with fewer than 7 consecutive days with default values available from 1979 to 2014 are analyzed. To ensure reliability and consistency of observations, we also use two monthly global land precipitation datasets based on rain gauges: the Climatic Research Unit (CRU) TS4.01 (Harris et al. 2014) and Global Precipitation Climatology Centre (GPCC) V7 (Schneider et al. 2014) datasets, as well as the Global Precipitation Climatology Project (GPCP) V2.3 global (land and ocean) precipitation dataset (Adler et al. 2003). Both CRU TS4.01 and GPCC V7 have a spatial resolution of 0.5° × 0.5° starting from 1901, and GPCP V2.3 has been on a 2.5° × 2.5° grid since 1979.

Monthly and daily atmospheric variables used in this study are obtained from the Japanese 55-yr Reanalysis (JRA-55) on a 1.25° × 1.25° horizontal resolution at 37 pressure levels, compiled by the Japan Meteorological Agency (Kobayashi et al. 2015; Harada et al. 2016). The variables include horizontal winds, vertical velocity, specific humidity, air temperature, and geopotential height. The European Centre for Medium-Range Weather Forecasts (ECMWF) interim reanalysis (ERA-Interim; Dee et al. 2011) with approximately 0.7° × 0.7° spatial resolution at 37 pressure levels is also used to verify the JRA-55 results. The monthly SST data are from NOAA Extended Reconstructed Sea Surface Temperature (ERSST) V5 on a 2° × 2° grid (Smith and Reynolds 2003). The period of above data is selected from 1979 to 2014 to match the length of the station data record. The topographic dataset used is from NOAA (http://www.ngdc.noaa.gov/mgg/topo/topo.html), and it is generated from a digital database of land and sea-floor elevations on a 5° × 5° grid.

b. Methods

The climatological monthly mean precipitation averaged over the HM during 1979–2014 is shown in Fig. 1b.

Consistent with Dong et al. (2018), the rainy seasons in the HM are defined from May to September, when the climatological monthly mean precipitation is above the annual mean over this region (Fig. 1b). The total precipitation during rainy seasons accounts for more than 80% of annual total precipitation.

To illustrate the propagation features of stationary Rossby wave train, we calculate the wave activity flux **W**, defined by Takaya and Nakamura (2001), as follows:

$$\mathbf{W} = \frac{1}{2|\overline{\mathbf{V}}|}\begin{Bmatrix} \overline{u}(\psi_x'^2 - \psi'\psi_{xx}') + \overline{v}(\psi_x'\psi_y' - \psi'\psi_{xy}') \\ \overline{u}(\psi_x'\psi_y' - \psi'\psi_{xy}') + \overline{v}(\psi_y'^2 - \psi'\psi_{yy}') \\ \dfrac{pf^2}{R\sigma}[\overline{u}(\psi_x'\psi_p' - \psi'\psi_{xp}') + \overline{v}(\psi_y'\psi_p' - \psi'\psi_{yp}')] \end{Bmatrix},$$

where overbars and primes denote climatology state and departure from the climatology state, respectively. Here $\mathbf{V} = (u,v)$ is the horizontal wind velocity, ψ is the streamfunction, f is the Coriolis parameter, R is the gas constant, and $\sigma = R\overline{T}/C_p p - d\overline{T}/dp$ is static stability, with T and C_p being the temperature and specific heat at constant pressure, respectively.

According to Yanai et al. (1973), the atmospheric apparent heat source Q_1 is used to represent the total diabatic heating (including radiation, latent heating, and surface heat flux),

$$Q_1 = C_p\frac{\partial T}{\partial t} - C_p(\omega\sigma - \mathbf{V}\cdot\nabla T),$$

where t is the time, ω is the vertical velocity, and $\sigma = RT/C_p p - \partial T/\partial p$ is the static stability. Circulation has a close relationship with heat source, and Q_1 is calculated to explore the effect of circulation–heating interaction.

Composite and correlation analysis are used, and the significance level is estimated based on the two-tailed Student's t test. Besides, a moving t test and Lepage test are adopted to detect abrupt changepoints in time series of precipitation over the HM. The Lepage test is a nonparametric, two-sample test for location and dispersion, and for significant differences between two samples, even if the distributions of parent populations are unknown (Lepage 1971). This method has been widely used to investigate climate change issues (Liu et al. 2011; Xu et al. 2015; Ha et al. 2016; Piao et al. 2017); a more detailed description can be found in the appendix. Here, a 7-yr window is used to identify the interdecadal changes for the moving t test and Lepage test. Note that the time window used for detection is not sensitive to the confirmation of changepoints, and a 9-yr window is also employed and shows similar results.

3. Results

a. *Interdecadal variation of precipitation in the HM*

Figure 2a shows area mean rainy-season precipitation anomalies averaged over the HM from 151 station observations for the period of 1979–2014. Significant interdecadal variations can be seen, and an obvious rainfall decrease occurs around 2004/05. The rainy-season precipitation is persistently close to or higher than normal before 2004/05 and below normal after 2004/05. Similar interdecadal changes of HM rainfall are also seen in CRU TS4.01 and GPCC V7 (see Figs. S1a and S1c in the online supplemental material).

To determine the abrupt changepoints of HM rainfall accurately, a moving t test and Lepage test are used, and the results are presented in Fig. 2b. Based on the 95% significance level, the results of the moving t test indicate the significant changepoints during 2002–06, whereas only 2005 is identified by the Lepage test. The same changepoint of 2005 is also obtained by using CRU TS4.01 and GPCC V7 (Figs. S1b,d). Furthermore, total occurrences of changepoints detected by reaching the 95% significance level for these two methods from 151 station observations, CRU TS4.01, and GPCC V7 are calculated (Fig. 2c). The year 2005 shows the highest occurrences and is confirmed in different precipitation datasets and detection methods, indicating the robustness of the HM rainfall decrease around 2004/05.

The 10-yr periods before and after the 2004/05 changepoint are chosen to calculate the differences in rainy-season precipitation. The spatial distribution of epochal differences in precipitation between 2005–14 and 1995–2004 derived from 151 station observations, CRU TS4.01, and GPCC V7 over the HM are shown in Fig. 3. The decadal decrease signals are not geographically homogeneous but vary from northeast to southwest. Large and significant precipitation deficits are observed over the southern HM (Fig. 3a). Highly similar rainfall change patterns are also obtained by CRU TS4.01, and GPCC V7 (Figs. 3b,c).

b. *Associated changes in atmospheric circulation and SST*

Consistent changes in atmospheric circulation are linked to the rainfall decrease. Figures 4a and 4b show the epochal differences in column-integrated moisture transport and 500-hPa vertical velocity respectively, both of which are key factors for precipitation (e.g., Hu et al. 2017; Tao et al. 2017; Dong et al. 2018).

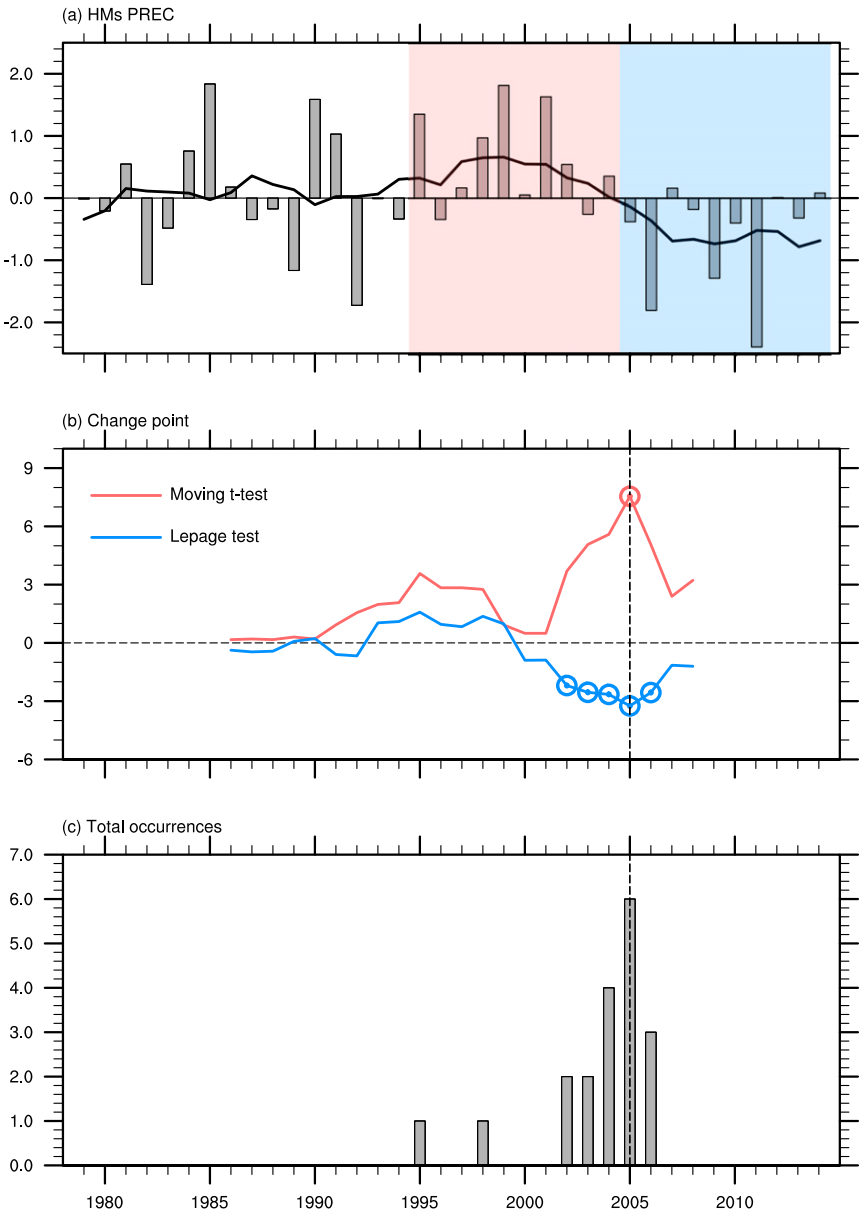

FIG. 2. (a) Time series of normalized rainy-season precipitation anomalies averaged over the HM from 151 station observations for the period of 1979–2014 (bar), and the corresponding interdecadal component calculated by removing the period shorter than 9 years (line). (b) Results of the moving *t* test (blue line) and Lepage test (red line) for the original time series shown in (a). (c) Total occurrences of changepoints detected by reaching the 95% significance level for the moving *t* test and Lepage test from 151 station observations, CRU TS4.01, and GPCC V7. Blue and red shadings in (a) represent 10-yr periods before and after the changepoint. Blue and red open circles in (b) indicate that the results of the moving *t* test and Lepage test, respectively, reach the 95% significance level in a particular year. Vertical dashed lines in (b) and (c) mark the changepoints in 2005.

Corresponding to the rainfall decrease over the southwestern HM, notable anomalous moisture divergence and downward motions extend along the southern foothills of the Himalayas (SFH) to the HM. A complete reduced rainfall belt over the SFH is clearly seen in Fig. 5a, which presents the epochal differences in global precipitation based on GPCP V2.3. The moisture is mainly confined at lower levels, so the spatial distribution

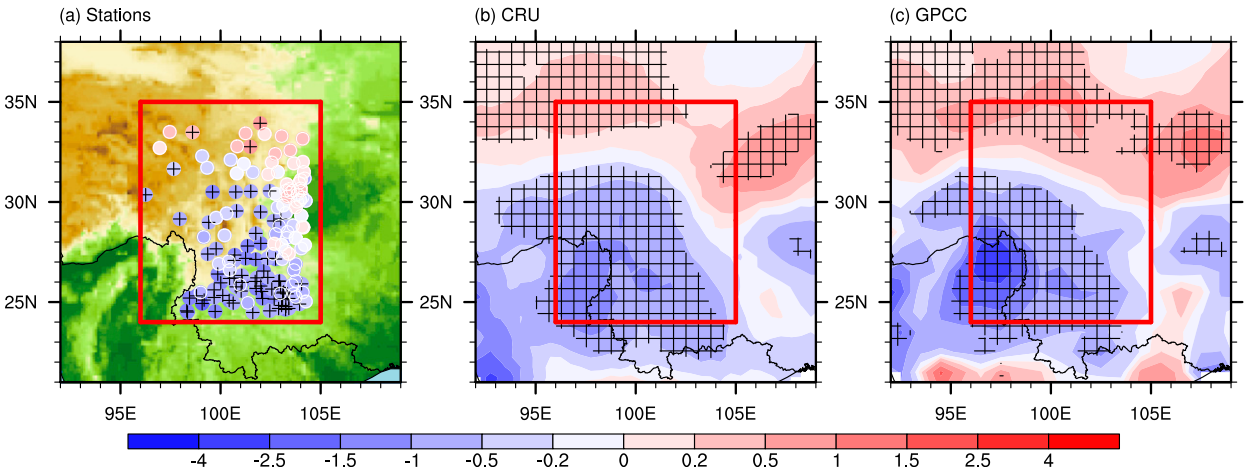

FIG. 3. Epochal differences (2005–14 minus 1995–2004) of rainy-season precipitation (mm) from (a) 151 station observations, (b) CRU TS4.01, and (c) GPCC V7. Cross marks in (a) and lattices in (b) and (c) indicate that the significance level reaches 90%.

of 850-hPa wind anomalies resembles that of moisture flux anomalies, and the moisture transport associated with easterly wind anomalies along the SFH favors the local divergence (Figs. 4a,c). The lower-level divergence and upper-level convergence cooperate well with midtropospheric descent over the SFH (Figs. 4b–d). At the south side of negative rainfall anomalies over the SFH, two large and significant centers of positive rainfall anomalies exhibit along the west coast of India (WCI) and over the Bay of Bengal (BOB), respectively (Fig. 5a). The associated distribution of changes in atmospheric circulation features two lower-level cyclones, as well as two centers of lower-level convergence, midtropospheric ascent, and upper-level divergence over the WCI and BOB (Figs. 4b–d).

As a result, the distribution of differences in rainfall manifests a dipole pattern, with dry anomalies along the SFH and wet anomalies in the area from the WCI to the BOB. Furthermore, their out-of-phase relationship is illustrated by constructing two rainfall indices, which are averaged over the SFH region and the WCI and BOB regions (Fig. 5b). The opposite temporal evolution of rainfall in these two areas exists on both the interannual and interdecadal time scale. Jiang and Ting (2017) found that the interannual variation of Indian subcontinent and TP rainfall exhibits a dipole pattern in which rainfall in the central and northern Indian subcontinent tends to be out of phase with that in the southeastern TP, while the long-term change is what we emphasize in present study.

The above analyses provide an overall picture of the dipole rainfall pattern and associated atmospheric circulation, and one prominent feature is the lower-level divergent easterly wind anomalies over the SFH (Fig. 4c). On one hand, the anomalous easterlies are accompanied by local moisture divergence and downward motions (Figs. 4a,b), leading to the dry anomalies there (Fig. 5a). On the other hand, the easterly wind anomalies appear at the northern edge of two cyclones, which are coupled with the dipole rainfall pattern (Figs. 4c and 5a). Note that the 850-hPa circulation changes around TP may be noisy due to topography. The whole pattern at 700 hPa has also been checked and is consistent with that at 850 hPa (figure not shown). However, the easterly wind anomalies and two anomalous cyclones are stronger at 850 hPa than 700 hPa, and thus 850 hPa is selected to better show the characteristics of lower-level circulation changes.

Some notable changes in atmospheric circulation over the Indo-Pacific sector are suggested to play important roles in wet anomalies over the area from the WCI to the BOB. At lower (upper) levels, the anomalous divergent (convergent) southerly (northerly) winds blowing from (to) the eastern Indian Ocean (EIO) contribute to the convergence (divergence) and upward motions over the India and BOB (Figs. 4b–f). Over the EIO, lower-level divergence (Figs. 4c,e), midtropospheric descent (Fig. 4b), and upper-level convergence (Figs. 4d,f) appear from the difference fields. They are accompanied by reverse circulation changes over the western Pacific (WP) and western Indian Ocean (WIO; Figs. 4b–f). Besides, as a Rossby wave response to suppressed rainfall anomalies over the EIO (Fig. 5a), the anomalous cross-equatorial anticyclonic winds bring abundant moisture from the ocean and cause the anomalous moisture convergence over the WCI and BOB (Figs. 4a,c), favoring the rainfall increase there. Note that the decadal changes in atmospheric circulation identified in JRA-55 are well matched with the observed rainfall changes, and similar

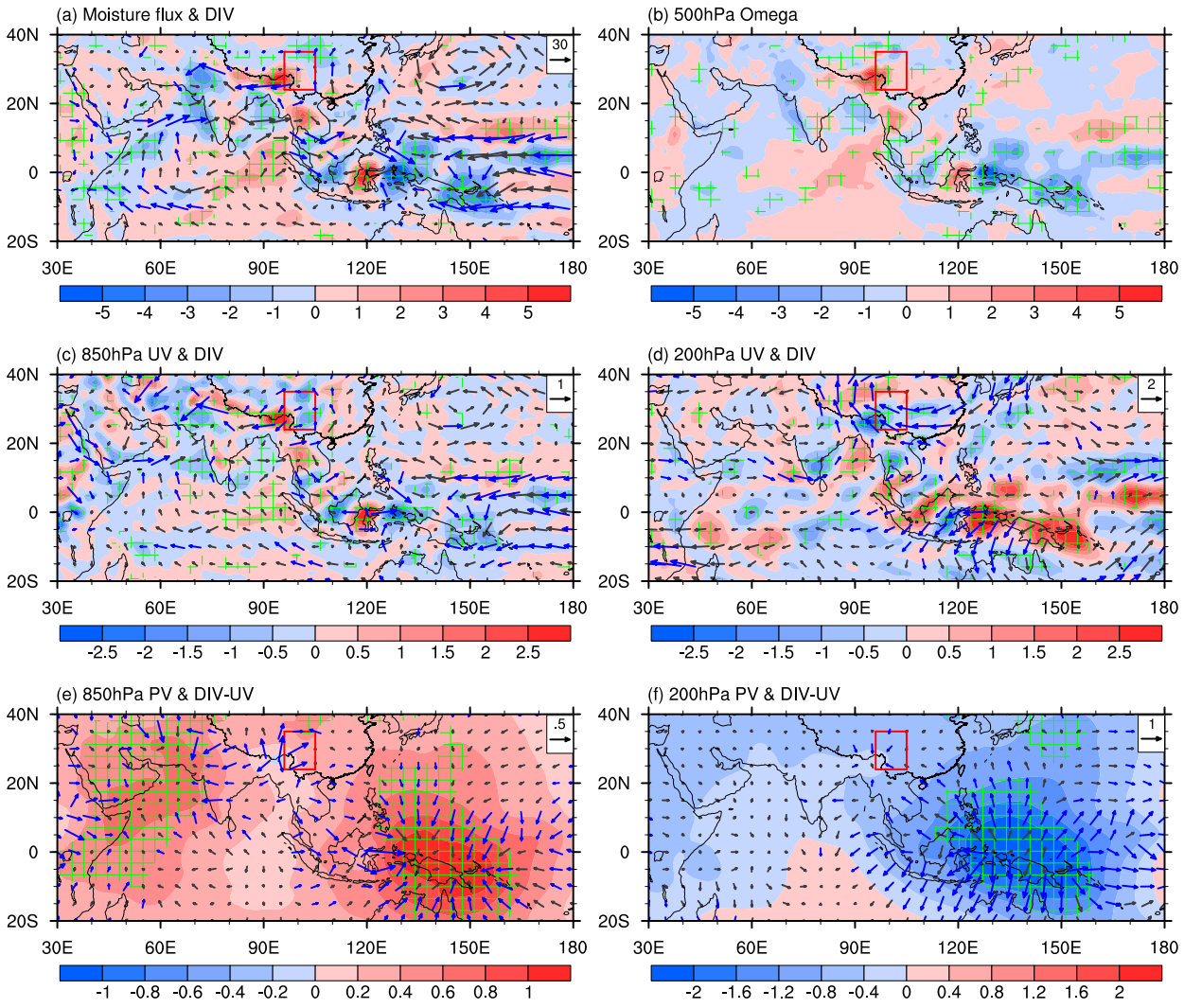

FIG. 4. Epochal differences (2005–14 minus 1995–2004) of rainy-season (a) column-integrated moisture flux (vector; $kg\,s^{-1}\,m^{-1}$) and moisture divergence (shaded; $10^{-5}\,kg\,s^{-1}\,m^{-1}$), (b) 500-hPa vertical velocity ($Pa\,s^{-1}$), (c) 850-hPa winds (vector; $m\,s^{-1}$) and divergence (shaded; $10^{-6}\,s^{-1}$), (d) 200-hPa winds (vector; $m\,s^{-1}$) and divergence (shaded; $10^{-6}\,s^{-1}$), (e) 850-hPa potential velocity (shaded; $10^{6}\,m^{2}\,s^{-1}$) and divergent winds (vector; $m\,s^{-1}$), and (f) 200-hPa potential velocity (shaded; $10^{6}\,m^{2}\,s^{-1}$) and divergent winds (vector; $m\,s^{-1}$) based on JRA-55. Lattices and blue vectors indicate that the significance level reaches 90%.

results are confirmed by difference fields based on ERA-Interim (Fig. S2), indicating the reliability of using reanalysis data to investigate regional climate change.

Atmospheric circulation over the Indo-Pacific sector is sensitive to the tropical ocean status, and Fig. 6a shows the epochal differences in rainy-season SST. Significant positive SST changes are seen in both the WP and Indian Ocean. Corresponding to the SST increase, rainfall is enhanced over the WP and WIO (Fig. 5a), with consistent changes in large-scale circulation as mentioned before (Figs. 4b–f). The anomalous rainfall and circulation over the EIO are more like the response of the WP and WIO SST changes, and the EIO SST warms up due to more downward shortwave radiation (Fig. 6b). Further, to examine the physical mechanism involved in WP and WIO SST affecting large-scale circulation and dipole rainfall pattern, solutions to atmospheric general circulation model (AGCM) are considered in the next subsection.

c. *Solutions to the AGCM*

The Max Plank Institute for Meteorology AGCM (ECHAM5.3.2) is used in this study, and we adopt a version with triangular truncation at zonal wavenumber 63 (T63; equivalent to 1.9° horizontal resolution) and 31 vertical levels extending to 10 hPa. More comprehensive

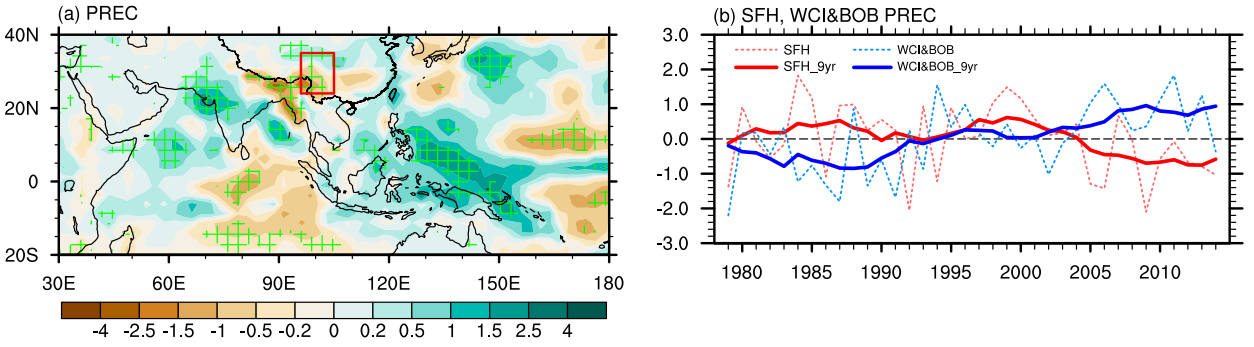

FIG. 5. (a) Epochal differences (2005–14 minus 1995–2004) of rainy-season precipitation (mm) from GPCP V2.3. (b) Time series of normalized rainy-season precipitation anomalies averaged over the SFH region (red dashed line; 22.5°–32.5°N, 80°–100°E) and the WCI and BOB regions (blue dashed line; WCI: 10°–32.5°N, 66.25°–78.75°E; BOB: 10°–20°N, 85°–95°E) from GPCP V2.3 for the period of 1979–2014, and the corresponding interdecadal component calculated by removing the period shorter than 9 years (solid lines). Lattices in (a) indicate that the significance level reaches 90%.

and detailed descriptions of this model can be found in Roeckner et al. (2003).

Three simulations are conducted with different boundary conditions. In the control run (CTRL), the model is forced by the observed monthly climatology of SST for 1995–2004. The other two experiments are designed with the epochal differences in monthly SST added to the climatological monthly SST during rainy seasons in the WP only (the WP run) or in both the WP and WIO (the WP&WIO run). In all experiments, the SST is kept constant in time and the model is integrated for 30 years. Thus, each simulation is equivalent to 30-member ensemble runs. Ensemble-mean results for rainy seasons are calculated as the departure from the CTRL run. The detailed information for the simulations is listed in Table 1.

In response to the positive SST anomalies over the WP, the convection is enhanced over the WP, especially the northwest Pacific, and suppressed from the Indian Ocean to the Maritime Continent (Fig. 7a). Correspondingly, the response of large-scale circulation exhibits a dipole pattern in the Indo-Pacific sector, with lower-level (upper-level) convergence (divergence) over the WP and divergence (convergence) over the Indian Ocean (Figs. 8a,b). Note that simulated positive rainfall anomalies with lower-level (upper-level) convergence (divergence) over the WP shift more northward than the observations and JRA-55 results (Figs. 4e,f, 5a, 7a, 8a,b). It seems that models overestimate the effect of SST anomalies in the Northern Hemisphere, where warming covers larger areas than the Southern Hemisphere. The cross-equatorial anticyclonic wind anomalies are weak and close to the central Indian Ocean. Although the dipole rainfall pattern is generally captured, only one anomalous cyclone appears over the BOB, and the easterly wind anomalies over the SFH are weaker than the JRA-55 results (Figs. 4c and 7a).

The simulations are closer to the observations and JRA-55 results when the additional WIO warming is added. The suppressed rainfall anomalies are realistically

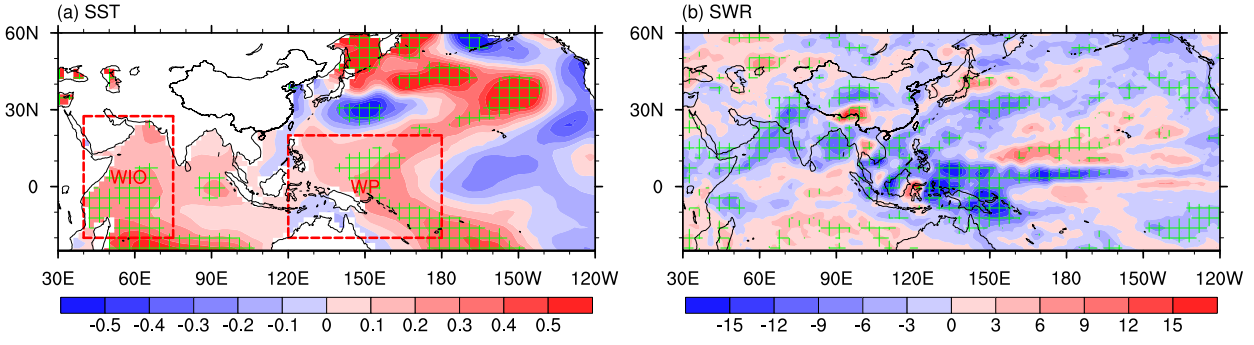

FIG. 6. Epochal differences (2005–14 minus 1995–2004) of rainy-season (a) SST (°C) from ERSST V5 and (b) surface net shortwave radiation (W m^{-2}; downward positive) from JRA-55. Lattices indicate that the significance level reaches 90%. The WP and WIO regions are outlined by the boxes in (a).

TABLE 1. List of the three ECHAM5.3.2 simulations: the CTRL run, WP run, and WP&WIO run.

Simulation	SST forcing field	Integration
CTRL	Global climatological SST for 1995–2004	30 years
WP	Added positive SST anomalies to climatological SST over 20°S–20°N, 120°E–180° (red dashed box over WP in Fig. 6a) from May to September	30 years
WP&WIO	Based on the WP run, added additional positive SST anomalies to climatological SST over 20°S–27.5°N, 40°E–75°E (red dashed box over WIO in Fig. 6a) from May to September	30 years

reproduced by the WP&WIO run (Figs. 5a and 7b), and the associated lower-level divergence and upper-level convergence resemble the JRA-55 results (Figs. 4e,f and 8c,d). Compared with the WP run, the cross-equatorial anticyclonic wind anomalies are strengthened and shift westward slightly, enhancing the rainfall near the WCI (Figs. 7a,b). The anomalous BOB cyclone and easterly wind anomalies over the SFH are also intensified, but the anomalous cyclone over the WCI still fails to be simulated. The simulated results of the WP&WIO run still underestimate the effect of WIO warming. The wet anomalies over the WIO are weaker than observations (Figs. 5a and 7b), with weaker lower-level convergence and upper-level divergence than the JRA-55 results (Figs. 4e,f and 8c,d). Besides, the biases of cross-equatorial anticyclonic wind anomalies in AGCM results are probably related to the weak WCI rainfall anomalies, since the westerly wind anomalies at southern edge of WCI cyclone are part of anomalous cross-equatorial anticyclonic winds in the JRA-55 results (Fig. 4c).

The above simulations reveal that the decadal changes of SST over the WP and WIO collaborate with each other and contribute to the dipole rainfall pattern. Moreover, the WP warming plays a more dominant role than WIO warming. Based on the WP warming, the additional WIO warming constrains the location of suppressed rainfall anomalies over the EIO through large-scale circulation adjustment (Figs. 7 and 8), and makes the simulations closer to the observations and JRA-55 results (Figs. 4c, 5a, and 7b). The rainfall and circulation response over the WP are stronger than over the WIO due to climatological SST, which is higher and more easily reaches the convective threshold in the WP (figure not shown). The EIO dry anomalies trigger the cross-equatorial anticyclonic wind anomalies as a Rossby wave response, and further cause anomalous meridional circulation and moisture transport over the WCI and BOB, favoring the rainfall increase there (Figs. 7 and 8). Although the dipole rainfall pattern is generally reproduced in AGCM, the detailed dynamical and thermodynamical processes involved in dipole rainfall pattern and associated anomalous circulation are still unclear, and we use a linear baroclinic model (LBM) to explore these questions in the next subsection. Note that model results exhibit weak rainfall anomalies over the WCI, especially the northern part, and the anomalous cyclone is not reproduced (Fig. 7). As shown in Figs. 4c and 4d, the decadal changes in wind fields over the WCI display a barotropic structure with anomalous lower- and upper-level cyclone, which may be related to atmospheric processes at middle and high latitudes and will be discussed in section 4.

d. Solutions to the LBM

The LBM built upon atmospheric primitive equations is used to examine the atmospheric response to heating (e.g., Annamalai et al. 2005; Xie et al. 2009; Tao et al.

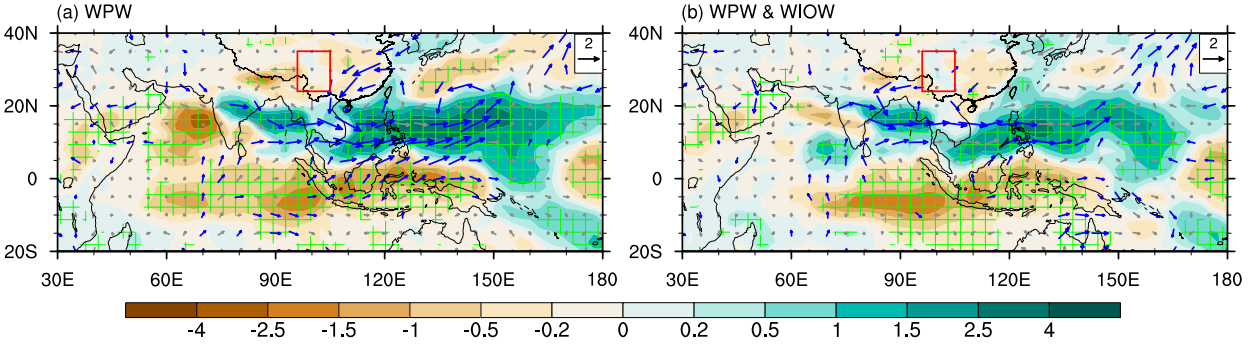

FIG. 7. Simulated rainy-season precipitation (shaded; mm) and 850-hPa wind (vector; m s^{-1}) anomalies: (a) WP minus CTRL run and (b) WP&WIO minus CTRL run.

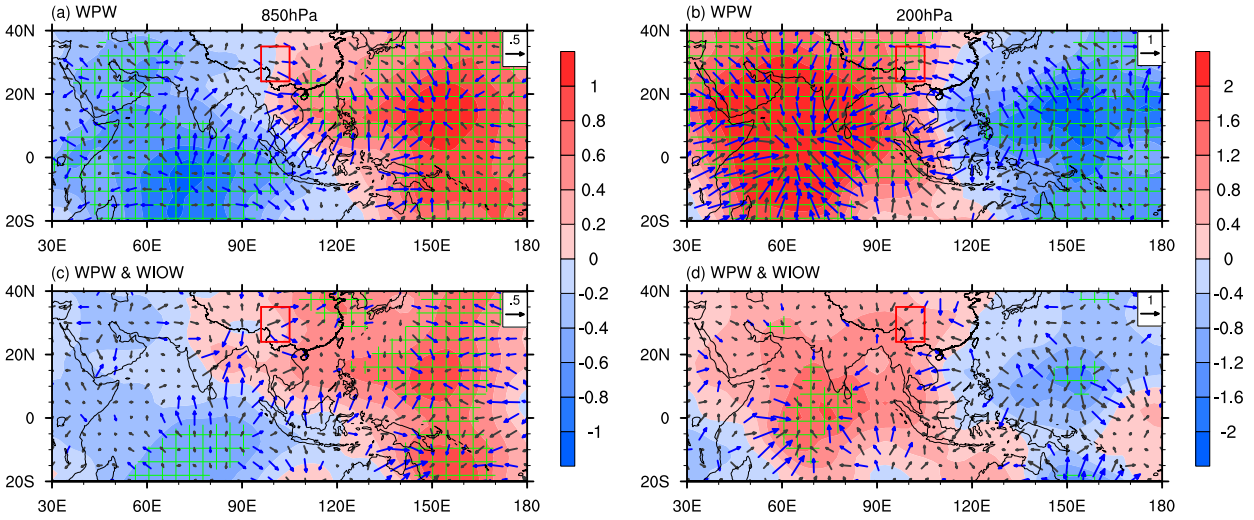

FIG. 8. Simulated rainy-season 850-hPa potential velocity (shaded; $10^6\,m^2\,s^{-1}$), 200-hPa potential velocity (shaded; $10^6\,m^2\,s^{-1}$), and relevant divergent winds (vector; $m\,s^{-1}$) anomalies: (top) WP minus CTRL run and (bottom) WP&WIO minus CTRL run.

2014; Qu and Huang 2016). We adopt a T42L20 dry version of LBM, which has a horizontal resolution of ~2.8° and 20 sigma levels in the vertical. The model employs horizontal and vertical diffusion, Rayleigh friction, and Newtonian damping. The horizontal diffusion has an *e*-folding decay time of 6 h for the largest wavenumber, and the vertical diffusion is set at $1000\,day^{-1}$ at all levels. The latter two terms have a time scale of $0.5\,day^{-1}$ for $\sigma \geq 0.9$ and $\sigma \leq 0.03$, and $20\,day^{-1}$ for $0.03 < \sigma < 0.9$. Besides, the component of steady forcing is included. More details are described in Watanabe and Jin (2002). Figure 9a presents the horizontal spatial distribution of epochal differences in Q_1. There are positive Q_1 anomalies along the WCI and over the BOB and negative Q_1 anomalies over the SFH, which are almost identical to the decadal changes of precipitation (Figs. 5a and 9a). The largest diabatic heating in each of these three regions is located at 300–500 hPa (Fig. 9b). To study the relative contribution of Q_1 in three regions to easterly divergent wind anomalies along the SFH, four experiments are conducted with observed Q_1 anomalies in the WCI, the BOB, the SFH,

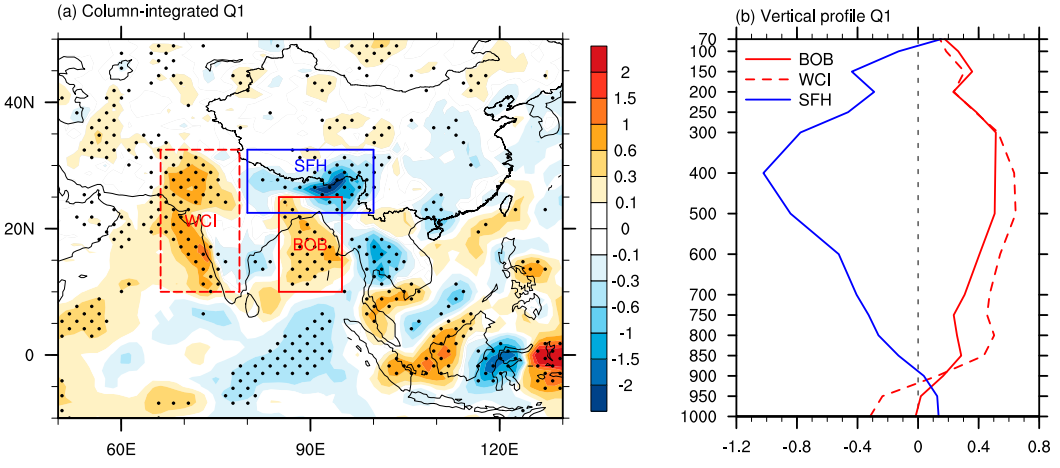

FIG. 9. (a) Epochal differences (2005–14 minus 1995–2004) of rainy-season diabatic heating ($K\,day^{-1}$) based on JRA-55. (b) Vertical profile of diabatic heating anomalies averaged over the positive value areas for WCI (10°–32.5°N, 66.25°–78.75°E), BOB (10°–25°N, 85°–95°E), and negative value areas for SFH (22.5°–32.5°N, 80°–100°E) in (a). Dots in (a) indicate that the significance level reaches 90%, and the WCI, BOB, and SFH regions are outlined by the boxes in (a).

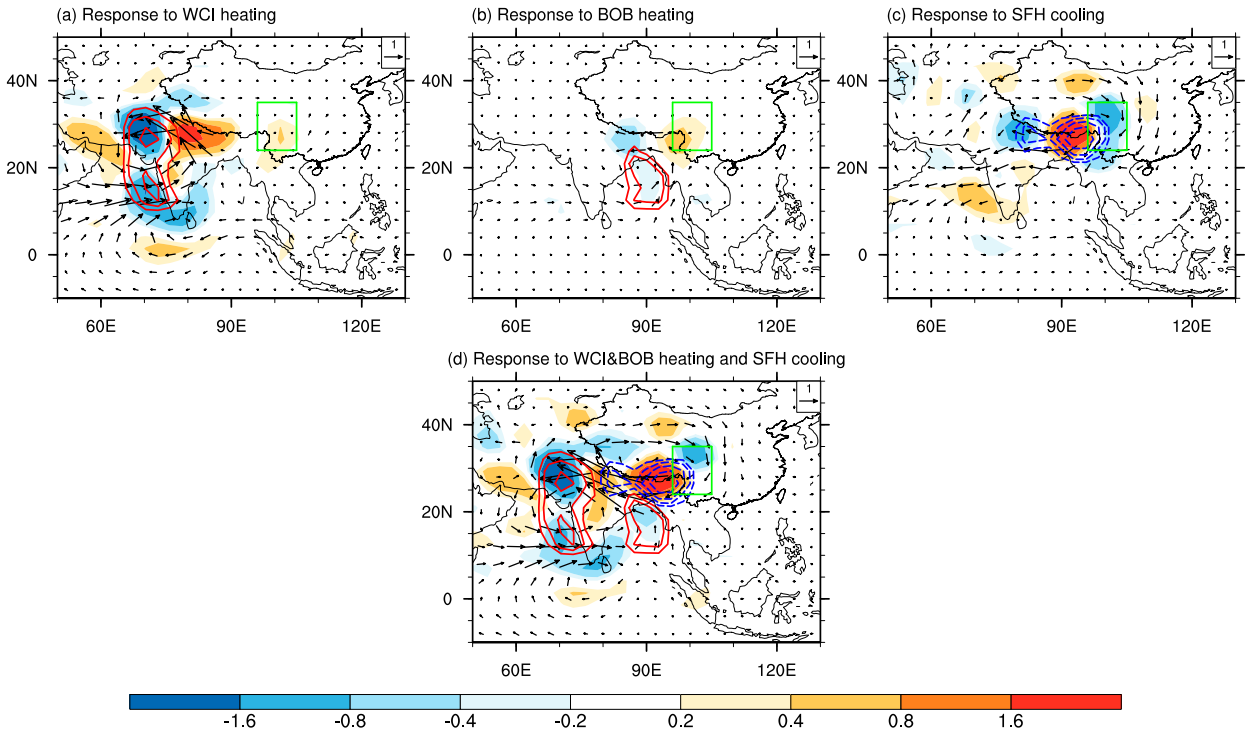

FIG. 10. The response of 850-hPa winds (vector; m s^{-1}) and divergence (shaded; 10^{-6} s^{-1}) to the observed diabatic heating anomalies (contour; ±0.1, ±0.3, ±0.6, ±1 K day^{-1}; negative contours are dashed) in (a) WCI, (b) BOB, (c) SFH, or (d) all regions imposed on the rainy season mean state for 1995–2004.

or in all regions imposed on the rainy season mean state for 1995–2004. The model is integrated for 50 days, and the response reaches equilibrium after 15 days, so the last 30 days' mean results are analyzed.

As shown in Fig. 10a, the positive rainfall anomalies–related heating anomalies in WCI trigger a strong cyclone over the Indian subcontinent as a response of warm Rossby wave. Correspondingly, anomalous lower-level easterly winds form over the southwestern TP and contribute to the local divergence anomalies. The circulation response seems weak over the SFH and HM at 850 hPa, and further inspection finds that the notable easterly wind and divergence anomalies extend along the SFH at 700 hPa (Fig. S3). The weak circulation response at 850 hPa along the SFH is probably due to no obvious heating anomalies over the northern WCI, but strong positive heating anomalies exist at 700 hPa (figure not shown). In response to the imposed positive heating anomalies in BOB, an anomalous cyclone develops to their northwestern side, and easterly wind anomalies appear over the SFH, leading to the divergence anomalies over the HM (Fig. 10b). The divergence anomalies in the above two experiments favor the reduction of precipitation along the SFH. Besides, the two anomalous cyclones also induce local convergence anomalies, and westerly wind anomalies at southern edge of cyclones increase moisture transport, both of which further favor the enhancement of rainfall anomalies over the WCI and BOB. These also document that the biases of cross-equatorial anticyclonic wind anomalies in AGCM results could be attributed to the weak simulation of WCI rainfall anomalies. The response of circulation anomalies to observed cooling anomalies over the SFH is examined in Fig. 10c, and the anomalous easterly winds over the SFH are dominant. The associated divergence anomalies near the HM further suppress precipitation there.

Figure 10d shows model results forced by the combination of heating anomalies in three regions. The spatial distribution of circulation anomalies highly resembles observed pattern, although the simulated anomalous BOB cyclone is slightly weaker than JRA-55 results (Figs. 4c and 10d). In general, the circulation response to heating anomalies is stronger at 850 than 700 hPa (Fig. 10; see also Fig. S3), consistent with the JRA-55 results. The above LBM experiments reveal the dynamical and thermodynamical processes involved in the dipole rainfall pattern and associated circulation anomalies, emphasizing the importance of circulation–heating interaction. On one hand, the anomalous

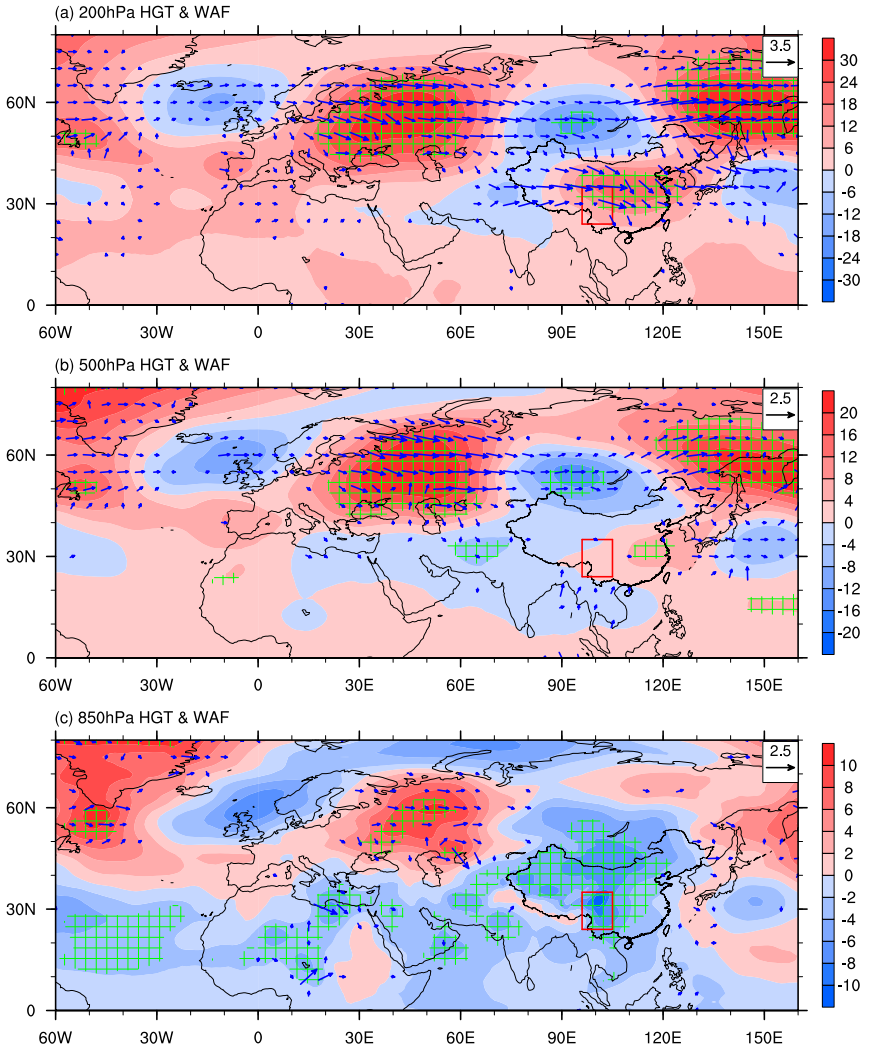

FIG. 11. Epochal differences (2005–14 minus 1995–2004) of rainy-season geopotential height (shaded; gpm) and horizontal component of wave activity fluxes (vectors; $m^2 s^{-2}$) at (a) 200, (b) 500, and (c) 850 hPa based on JRA-55. Dots indicate that the significance level reaches 90%, and arrows with magnitudes less than 0.3 are omitted.

easterlies at the northern edge of two cyclones induced by the wet anomalies–related heating cause the divergence anomalies along the SFH, favoring the reduction of precipitation there. On the other hand, the two anomalous cyclones and dry anomalies have positive feedback on wet and easterly wind anomalies, respectively.

4. Discussion

The WCI wet anomalies and associated anomalous lower-level cyclone are not well reproduced in AGCM experiments, which are forced by positive SST anomalies over the WP and WIO (Fig. 7b). Moreover, abundant studies indicate that the atmospheric processes at middle and high latitudes could affect Indian summer monsoon rainfall (e.g., Lau et al. 2000; Lu et al. 2002; Ding and Wang 2005; Goswami et al. 2006; Ding and Wang 2007; Lau and Kim 2012; Gong et al. 2017; Wang et al. 2017). Figure 11 illustrates the decadal changes in geopotential height and wave activity fluxes at 200, 500, and 850 hPa. The lower-level anomalous WCI cyclone is accompanied by low pressure anomalies (Figs. 4c and 11c). At upper levels, the anomalous cyclone and low pressure center shift slightly northward to Pakistan and northern India (Figs. 4d and 11a,b). The northern part of the WCI rainfall anomalies corresponds well with the anomalous low pressure

circulation system, which displays a barotropic structure (Figs. 4c,d, 5a, and 11a–c).

Additionally, two zonally oriented barotropic wave trains are observed: one is trapped along the subtropical Asian jet stream, and the other is emanating from the British Isles, across northern Scandinavia to Mongolia. The whole structure closely resembles the interdecadal component of the SRP (Fig. 4 of Wang et al. 2017). Thus, the interdecadal change of the SRP affects the low pressure circulation anomalies near WCI, which mainly contribute to northern part of WCI wet anomalies. Note that the northern branch of the wave trains is also captured on intraseasonal time scale during boreal summer [see Figs. 3 and 4 of Nakamura and Fukamachi (2004) and Figs. 7 and 14 of Iwao and Takahashi (2008)]. Wang et al. (2017) explained that the appearance of this wave train on an interdecadal time scale might arise from the efficient modulation of the interdecadal background flow on a preferred phase of the intraseasonal wave train. Similar features of decadal changes in geopotential height and wave activity fluxes are also captured by ERA-Interim (Fig. S4).

An interdecadal change occurs in the summertime SRP index, which switches into its negative phase after the late 1990s [see Fig. 2 of Hong et al. (2017) and Figs. 2 and 3 of Wang et al. (2017)]. The same changepoint is identified in rainy-season SRP index, which is calculated by using different averaging months (Fig. S5). The SST changes over the WP and WIO are also critical in contributing to HM rainfall, as demonstrated by both observations and numerical experiments. The temporal evolutions of SST changes in these two regions both exhibit long-term warming trends (Fig. S5). However, the HM rainy-season rainfall experienced a distinct interdecadal change around 2004/05. The timing of the interdecadal transition in SST and SRP is not consistent with that of the HM rainfall, and it seems to exclude the single effect of any factor and emphasize their combined effect. Furthermore, the LBM results show that the local circulation–heating interaction is also critical in affecting the signal of the interdecadal changes induced by remote forcing.

Further analysis of reasons causing the interdecadal changes of SST in the two regions and SRP is beyond the scope of this study and only briefly discussed here. Note that the epochal differences in SST to some extent manifested as a PDO-like pattern (Fig. 6a). The PDO switches to its cold phase around 2000, coupled with an enhanced zonal SST gradient and accelerated trade wind in the equatorial Pacific. Such changes drive additional heat into the WP, resulting the warming there (Maher et al. 2018). The SST changes over the Indian Ocean are chiefly attributed to anthropogenic forcing and PDO modulation (Du and Xie 2008; Dong et al. 2013; Yao et al. 2016; Dong and McPhaden 2017a,b; Yao et al. 2017). Beside the Indo-western Pacific warming, significant warming is also identified over the tropical Atlantic (figure not shown). The Atlantic warming intensifies Indo-western Pacific warming by driving anomalous easterlies there as a Kelvin wave response and through the wind–evaporation–SST effect (Li et al. 2015; Kamae et al. 2017). Xu et al. (2015) proposed that the tropical Atlantic warming plays an important role in the rainfall reduction over southern and southwestern China via inducing wave trains over Eurasia. However, the experiment forced by tropical Atlantic warming cannot reproduce the SRP-like pattern, probably due to the different forcing months and regions in present study (figures not shown). Previous studies suggest that the AMO may modulate its interdecadal changes (Wu et al. 2016; Hong et al. 2017). However, Wang et al. (2017) found that the linear relationship between the AMO and SRP is not significant, and that the Monte Carlo bootstrapping resampling analysis implies that spring and summer AMO have plausible prediction potential for the interdecadal SRP.

5. Summary

In this study, the interdecadal variation of precipitation over the HM during rainy seasons is investigated based on various observational and reanalysis datasets. Rainy-season precipitation in HM experiences an obvious interdecadal change around 2004/05 identified by the moving t test and Lepage test. The precipitation there is persistently close to or higher than normal during 1995–2004 and below normal during 2005–14. According to the differences in rainy-season precipitation for these two periods, large and significant precipitation deficits are observed over the southern HM.

Changes in atmospheric circulation accompanying the rainfall decrease are summarized as follows. One prominent feature is the lower-level easterly wind anomalies extending along the SFH to the HM, which are coherent with anomalous moisture divergence and downward motions, and favor the rainfall decrease there. The divergent easterly wind anomalies appear at the northern edge of two anomalous cyclones over the WCI and BOB, corresponding well with the two centers of positive rainfall anomalies. Thus, the dry anomalies along SFH and the wet anomalies extending from WCI to BOB form a dipole rainfall pattern, which is accompanied by two anomalous cyclones.

The formation of wet anomalies over the WCI and BOB is highly related to the anomalous divergent

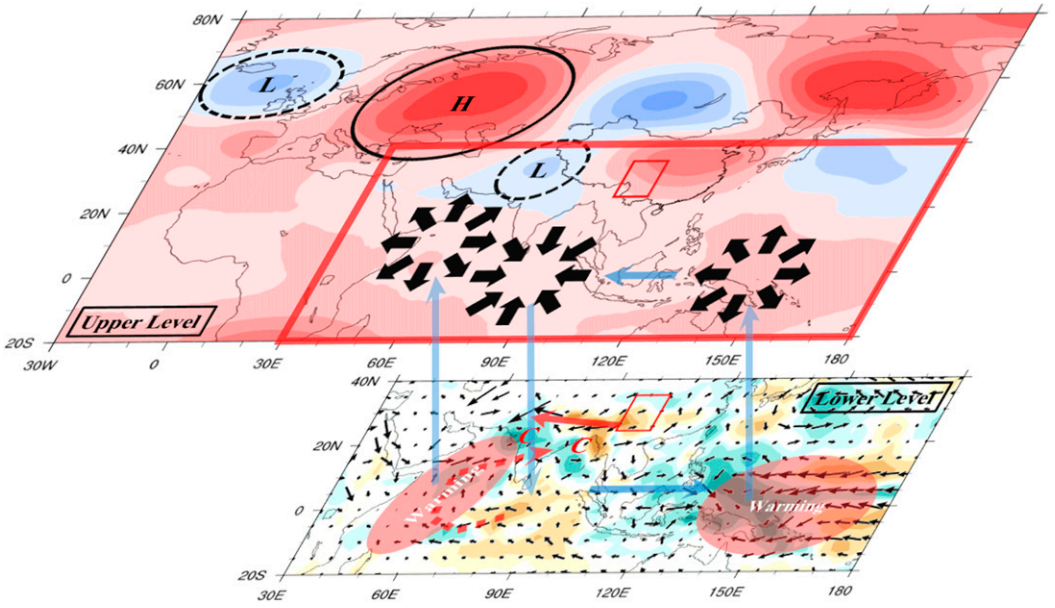

FIG. 12. Schematic diagram illustrating the main mechanisms involved in decadal SST and SRP changes affecting the precipitation over the HM during rainy seasons. (bottom) Epochal differences (2005–14 minus 1995–2004) of rainy-season precipitation (shaded; mm) from GPCP V2.3 and 850-hPa wind (vector; m s^{-1}) from JRA-55. (top) Epochal differences of rainy-season geopotential height (gpm) at 200 hPa from JRA-55. The HM region is marked by a red box. Red shadings over the WP and WIO represent positive SST anomalies there. Blue arrows represent the large-scale circulation adjustment. Black arrows represent the upper-level convergence and divergence. Red dashed arrows represent lower-level cross-equatorial anticyclonic wind anomalies triggered by negative precipitation anomalies over the EIO as a Rossby wave response. The "H" and "L" in black circles represent anomalous high and low pressure at upper levels. Two letters "C" mark the location of two anomalous lower-level cyclones. Red arrows represent lower-level easterly wind anomalies along the SFH.

(convergent) southerly (northerly) winds blowing from (to) the EIO at lower (upper) levels. There are lower-level divergence, midtropospheric descent, and upper-level convergence over the EIO, accompanying by reverse circulation changes over the WP and WIO. Numerical experiments document that the positive SST anomalies in WP and WIO suppress rainfall over the EIO through large-scale circulation adjustment. The EIO dry anomalies trigger the cross-equatorial anticyclonic wind anomalies as a Rossby wave response, and further cause anomalous meridional circulation and moisture transport over the WCI and BOB, favoring the rainfall increase there. Note that the northern part of WCI wet anomalies is poorly simulated in numerical experiments and cannot be well explained by the SST changes. The interdecadal change of SRP could affect the low pressure circulation anomalies near WCI via wave train, and mainly contributes to the northern part of the WCI wet anomalies. Figure 12 gives the schematic diagram, illustrating that the combined effects of decadal changes in SST and SRP influence the circulation and further HM precipitation during rainy seasons.

Further, LBM experiments reveal the detailed dynamical and thermodynamical processes involved in dipole rainfall pattern and associated circulation anomalies, emphasizing the importance of circulation-heating interaction. On one hand, the anomalous easterlies at the northern edge of two cyclones induced by the wet anomalies–related heating cause the divergence anomalies along the SFH, favoring the reduction of rainfall there. On the other hand, the two anomalous cyclones and dry anomalies have positive feedback on wet and easterly wind anomalies, respectively.

Acknowledgments. We thank two anonymous reviewers as well as the editor for their useful comments. This work was supported by the Strategic Priority Research Program of Chinese Academy of Sciences (XDA20060501), the National Key R&D Program of China (2018YFA0605904), the National Natural Science Foundation of China (41705068, 41831175, 41425019 and 41721004), and the China Postdoctoral Science Foundation (2016LH0005 and 2016M600116).

APPENDIX

Lepage Test

Using a combination of standardized Wilcoxon's and Ansari-Bradley's statistics, the Lepage test statistic [HK; symbol defined by Yonetani and McCabe (1994)] is calculated as

$$\mathrm{HK} = \frac{[W - E(W)]^2}{V(W)} + \frac{[A - E(A)]^2}{V(A)}.$$

It follows the chi-square distribution with two degrees of freedom. If HK exceeds 9.21 (5.99, 4.21), then the difference between two sample means corresponds to a significant confidence level of 99% (95%, 90%). A series $XY(x_1, x_2, \ldots, x_{n_1}, y_1, y_2, \ldots, y_{n_2})$ is composed of two independent series $X(x_1, x_2, \ldots, x_{n_1})$ and $Y(y_1, y_2, \ldots, y_{n_2})$ with sizes n_1 and n_2, respectively. Assume that $u_i = 0$ ($u_i = 0$) if the ith smallest data point in XY belongs to X (Y). The statistics for HK can be derived based on the following empirical formulas:

$$W = \sum_{i=1}^{n_1+n_2} i\mu_i,$$

$$E(W) = \frac{n_1(n_1 + n_2 + 1)}{2},$$

$$V(W) = \frac{n_1 n_2(n_1 + n_2 + 1)}{2},$$

$$A = \sum_{i=1}^{n_1} i\mu_i + \sum_{i=n_1+1}^{n_1+n_2} (n_1 + n_2 - i + 1)\mu_i,$$

$$E(A) = \frac{n_1(n_1 + n_2 + 2)}{4}, \quad \text{and}$$

$$V(A) = \frac{n_1 n_2(n_1 + n_2 - 2)(n_1 + n_2 + 2)}{48(n_1 + n_2 - 1)}.$$

Intervals of data along each time series are compared in the following manner: data for N years previous to a specified year Y_c (sample X) are compared to the data for year Y_c plus the $N - 1$ years following year Y_c (sample Y). The year Y_c is moved successively at 1-yr increments along the time series, and the Lepage test is conducted for each year Y_c.

REFERENCES

Adler, R. F., and Coauthors, 2003: The version-2 Global Precipitation Climatology Project (GPCP) monthly precipitation analysis (1979–present). *J. Hydrometeor.*, **4**, 1147–1167, https://doi.org/10.1175/1525-7541(2003)004<1147:TVGPCP>2.0.CO;2.

Annamalai, H., S. P. Xie, J. P. McCreary, and R. Murtugudde, 2005: Impact of Indian Ocean sea surface temperature on developing El Niño. *J. Climate*, **18**, 302–319, https://doi.org/10.1175/JCLI-3268.1.

Chen, J., Z. Wen, R. Wu, Z. Chen, and P. Zhao, 2014: Interdecadal changes in the relationship between southern China winter–spring precipitation and ENSO. *Climate Dyn.*, **43**, 1327–1338, https://doi.org/10.1007/s00382-013-1947-x.

——, ——, ——, X. Wang, C. He, and Z. Chen, 2017: An interdecadal change in the intensity of interannual variability in summer rainfall over southern China around early 1990s. *Climate Dyn.*, **48**, 191–207, https://doi.org/10.1007/s00382-016-3069-8.

Cheng, Z., C. Weng, J. Guo, L. Dai, and Z. Zhou, 2018: Vegetation responses to late Quaternary climate change in a biodiversity hotspot, the Three Parallel Rivers region in southwestern China. *Palaeogeogr. Palaeoclimatol. Palaeoecol.*, **491**, 10–20, https://doi.org/10.1016/j.palaeo.2017.11.032.

Dai, E., Y. Wang, L. Ma, L. Yin, and Z. Wu, 2018: 'Urban-rural' gradient analysis of landscape changes around cities in mountainous regions: A case study of the Hengduan Mountain region in Southwest China. *Sustainability*, **10**, 1019, https://doi.org/10.3390/su10041019.

Dee, D. P., and Coauthors, 2011: The ERA-Interim reanalysis: Configuration and performance of the data assimilation system. *Quart. J. Roy. Meteor. Soc.*, **137**, 553–597, https://doi.org/10.1002/qj.828.

Ding, Q., and B. Wang, 2005: Circumglobal teleconnection in the Northern Hemisphere summer. *J. Climate*, **18**, 3483–3505, https://doi.org/10.1175/JCLI3473.1.

——, and ——, 2007: Intraseasonal teleconnection between the summer Eurasian wave train and the Indian monsoon. *J. Climate*, **20**, 3751–3767, https://doi.org/10.1175/JCLI4221.1.

Ding, Y., Z. Wang, and Y. Sun, 2008: Inter-decadal variation of the summer precipitation in East China and its association with decreasing Asian summer monsoon. Part I: Observed evidences. *Int. J. Climatol.*, **28**, 1139–1161, https://doi.org/10.1002/joc.1615.

Dong, D., G. Huang, W. Tao, R. Wu, K. Hu, and C. Li, 2018: Interannual variation of precipitation over the Hengduan Mountains during rainy season. *Int. J. Climatol.*, **38**, 2112–2125, https://doi.org/10.1002/joc.5321.

Dong, L., and M. J. McPhaden, 2017a: The effects of external forcing and internal variability on the formation of interhemispheric sea surface temperature gradient trends in the Indian Ocean. *J. Climate*, **30**, 9077–9095, https://doi.org/10.1175/JCLI-D-17-0138.1.

——, and ——, 2017b: Why has the relationship between Indian and Pacific Ocean decadal variability changed in recent decades? *J. Climate*, **30**, 1971–1983, https://doi.org/10.1175/JCLI-D-16-0313.1.

——, T. Zhou, and B. Wu, 2013: Indian Ocean warming during 1958–2004 simulated by a climate system model and its mechanism. *Climate Dyn.*, **42**, 203–217, https://doi.org/10.1007/s00382-013-1722-z.

Dong, W., and Coauthors, 2016: Summer rainfall over the southwestern Tibetan Plateau controlled by deep convection over the Indian subcontinent. *Nat. Commun.*, **7**, 10925, https://doi.org/10.1038/ncomms10925.

Du, Y., and S.-P. Xie, 2008: Role of atmospheric adjustments in the tropical Indian Ocean warming during the 20th century in climate models. *Geophys. Res. Lett.*, **35**, L08712, https://doi.org/10.1029/2008GL033631.

Enomoto, T., B. J. Hoskins, and Y. Matsuda, 2003: The formation mechanism of the Bonin high in August. *Quart. J. Roy. Meteor. Soc.*, **129**, 157–178, https://doi.org/10.1256/qj.01.211.

Fang, S., Y. Zhao, L. Han, and C. Ma, 2017: Analysis of landscape patterns of arid valleys in China, based on grain size effect. *Sustainability*, **9**, 2263, https://doi.org/10.3390/su9122263.

Gong, D.-Y., and C.-H. Ho, 2002: Shift in the summer rainfall over the Yangtze River valley in the late 1970s. *Geophys. Res. Lett.*, **29**, 1436, https://doi.org/10.1029/2001GL014523.

——, D. Guo, S. Li, and S.-J. Kim, 2017: Winter AO/NAO modifies summer ocean heat content and monsoonal circulation over the western Indian Ocean. *J. Meteor. Res.*, **31**, 94–106, https://doi.org/10.1007/s13351-017-6175-6.

Gong, Z., G. Feng, M. M. Dogar, and G. Huang, 2018: The possible physical mechanism for the EAP–SR co-action. *Climate Dyn.*, **51**, 1499–1516, https://doi.org/10.1007/s00382-017-3967-4.

Goswami, B. N., M. S. Madhusoodanan, C. P. Neema, and D. Sengupta, 2006: A physical mechanism for North Atlantic SST influence on the Indian summer monsoon. *Geophys. Res. Lett.*, **33**, L02706, https://doi.org/10.1029/2005GL024803.

Ha, Y., Z. Zhong, H. Chen, and Y. Hu, 2016: Out-of-phase decadal changes in boreal summer rainfall between Yellow-Huaihe River Valley and southern China around 2002/2003. *Climate Dyn.*, **47**, 137–158, https://doi.org/10.1007/s00382-015-2828-2.

Harada, Y., and Coauthors, 2016: The JRA-55 Reanalysis: Representation of atmospheric circulation and climate variability. *J. Meteor. Soc. Japan*, **94**, 269–302, https://doi.org/10.2151/jmsj.2016-015.

Harris, I., P. D. Jones, T. J. Osborn, and D. H. Lister, 2014: Updated high-resolution grids of monthly climatic observations—The CRU TS3.10 dataset. *Int. J. Climatol.*, **34**, 623–642, https://doi.org/10.1002/joc.3711.

Hong, X., and R. Lu, 2016: The meridional displacement of the summer Asian jet, Silk Road pattern, and tropical SST anomalies. *J. Climate*, **29**, 3753–3766, https://doi.org/10.1175/JCLI-D-15-0541.1.

——, ——, and S. Li, 2017: Amplified summer warming in Europe–West Asia and Northeast Asia after the mid-1990s. *Environ. Res. Lett.*, **12**, 094007, https://doi.org/10.1088/1748-9326/aa7909.

Hu, K., S.-P. Xie, and G. Huang, 2017: Orographically anchored El Niño effect on summer rainfall in central China. *J. Climate*, **30**, 10 037–10 045, https://doi.org/10.1175/JCLI-D-17-0312.1.

Hu, Z.-Z., 1997: Interdecadal variability of summer climate over East Asia and its association with 500 hPa height and global sea surface temperature. *J. Geophys. Res.*, **102**, 19 403–19 412, https://doi.org/10.1029/97JD01052.

Hua, L., L. Zhong, and Z. Ma, 2017: Decadal transition of moisture sources and transport in northwestern China during summer from 1982 to 2010. *J. Geophys. Res. Atmos.*, **122**, 12 522–12 540, https://doi.org/10.1002/2017JD027728.

Huang, R., Y. Liu, and T. Feng, 2013: Interdecadal change of summer precipitation over eastern China around the late-1990s and associated circulation anomalies, internal dynamical causes. *Chin. Sci. Bull.*, **58**, 1339–1349, https://doi.org/10.1007/s11434-012-5545-9.

Iwao, K., and M. Takahashi, 2008: A precipitation seesaw mode between Northeast Asia and Siberia in summer caused by Rossby waves over the Eurasian continent. *J. Climate*, **21**, 2401–2419, https://doi.org/10.1175/2007JCLI1949.1.

Jiang, X., and M. Ting, 2017: A dipole pattern of summertime rainfall across the Indian subcontinent and the Tibetan Plateau. *J. Climate*, **30**, 9607–9620, https://doi.org/10.1175/JCLI-D-16-0914.1.

Kamae, Y., X. Li, S.-P. Xie, and H. Ueda, 2017: Atlantic effects on recent decadal trends in global monsoon. *Climate Dyn.*, **49**, 3443–3455, https://doi.org/10.1007/s00382-017-3522-3.

Kobayashi, S., and Coauthors, 2015: The JRA-55 Reanalysis: General specifications and basic characteristics. *J. Meteor. Soc. Japan*, **93**, 5–48, https://doi.org/10.2151/jmsj.2015-001.

Kosaka, Y., H. Nakamura, M. Watanabe, and M. Kimoto, 2009: Analysis on the dynamics of a wave-like teleconnection pattern along the summertime Asian jet based on a reanalysis dataset and climate model simulations. *J. Meteor. Soc. Japan*, **87**, 561–580, https://doi.org/10.2151/jmsj.87.561.

Lau, K.-M., K.-M. Kim, and S. Yang, 2000: Dynamical and boundary forcing characteristics of regional components of the Asian summer monsoon. *J. Climate*, **13**, 2461–2482, https://doi.org/10.1175/1520-0442(2000)013<2461:DABFCO>2.0.CO;2.

Lau, W. K. M., and K.-M. Kim, 2012: The 2010 Pakistan flood and Russian heat wave: Teleconnection of hydrometeorological extremes. *J. Hydrometeor.*, **13**, 392–403, https://doi.org/10.1175/JHM-D-11-016.1.

Lepage, Y., 1971: A combination of Wilcoxon's and Ansari-Bradley's statistics. *Biometrika*, **58**, 213–217, https://doi.org/10.1093/biomet/58.1.213.

Li, H., A. Dai, T. Zhou, and J. Lu, 2010: Responses of East Asian summer monsoon to historical SST and atmospheric forcing during 1950–2000. *Climate Dyn.*, **34**, 501–514, https://doi.org/10.1007/s00382-008-0482-7.

Li, X., S.-P. Xie, S. T. Gille, and C. Yoo, 2015: Atlantic-induced pan-tropical climate change over the past three decades. *Nat. Climate Change*, **6**, 275–279, https://doi.org/10.1038/nclimate2840.

Li, Z., Y. He, C. Wang, X. Wang, H. Xin, W. Zhang, and W. Cao, 2011: Spatial and temporal trends of temperature and precipitation during 1960–2008 at the Hengduan Mountains, China. *Quat. Int.*, **236**, 127–142, https://doi.org/10.1016/j.quaint.2010.05.017.

Liu, Y., G. Huang, and R. Huang, 2011: Inter-decadal variability of summer rainfall in Eastern China detected by the Lepage test. *Theor. Appl. Climatol.*, **106**, 481–488, https://doi.org/10.1007/s00704-011-0442-8.

Lu, R.-Y., J.-H. Oh, and B.-J. Kim, 2002: A teleconnection pattern in upper-level meridional wind over the North African and Eurasian continent in summer. *Tellus*, **54A**, 44–55, https://doi.org/10.1034/j.1600-0870.2002.00248.x.

Ma, Z., 2007: The interdecadal trend and shift of dry/wet over the central part of North China and their relationship to the Pacific decadal oscillation (PDO). *Chin. Sci. Bull.*, **52**, 2130–2139, https://doi.org/10.1007/s11434-007-0284-z.

Maher, N., M. H. England, A. Sen Gupta, and P. Spence, 2018: Role of Pacific trade winds in driving ocean temperatures during the recent slowdown and projections under a wind trend reversal. *Climate Dyn.*, **51**, 321–336, https://doi.org/10.1007/s00382-017-3923-3.

Nakamura, H., and T. Fukamachi, 2004: Evolution and dynamics of summertime blocking over the Far East and the associated surface Okhotsk high. *Quart. J. Roy. Meteor. Soc.*, **130**, 1213–1233, https://doi.org/10.1256/qj.03.101.

Nie, Z. L., Z. J. Gu, and H. Sun, 2002: Cytological study of *Tibetia* (Fabaceae) in the Hengduan Mountains region, China. *J. Plant Res.*, **115**, 17–22, https://doi.org/10.1007/s102650200003.

Piao, J., W. Chen, K. Wei, Y. Liu, H.-F. Graf, J.-B. Ahn, and A. Pogoreltsev, 2017: An abrupt rainfall decrease over the

Asian inland plateau region around 1999 and the possible underlying mechanism. *Adv. Atmos. Sci.*, **34**, 456–468, https://doi.org/10.1007/s00376-016-6136-5.

——, ——, S. Chen, and K. Wei, 2018: Intensified impact of North Atlantic Oscillation in May on subsequent July Asian inland plateau precipitation since the late 1970s. *Int. J. Climatol.*, **38**, 2605–2612, https://doi.org/10.1002/joc.5332.

Qian, C., and T. Zhou, 2014: Multidecadal variability of north China aridity and its relationship to PDO during 1900–2010. *J. Climate*, **27**, 1210–1222, https://doi.org/10.1175/JCLI-D-13-00235.1.

——, J.-Y. Yu, and G. Chen, 2014: Decadal summer drought frequency in China: The increasing influence of the Atlantic Multi-decadal Oscillation. *Environ. Res. Lett.*, **9**, 124004, https://doi.org/10.1088/1748-9326/9/12/124004.

Qu, X., and G. Huang, 2016: The global warming–induced South Asian high change and its uncertainty. *J. Climate*, **29**, 2259–2273, https://doi.org/10.1175/JCLI-D-15-0638.1.

Ren, Y., L. Song, Z. Wang, Y. Xiao, and B. Zhou, 2017: A possible abrupt change in summer precipitation over eastern China around 2009. *J. Meteor. Res.*, **31**, 397–408, https://doi.org/10.1007/s13351-016-6021-2.

Roeckner, E., and Coauthors, 2003: Atmospheric general circulation model ECHAM5: Part I. Max-Planck-Institute for Meteorology Rep. 349, 140 pp., https://www.mpimet.mpg.de/fileadmin/publikationen/Reports/max_scirep_349.pdf.

Schneider, U., A. Becker, P. Finger, A. Meyer-Christoffer, M. Ziese, and B. Rudolf, 2014: GPCC's new land surface precipitation climatology based on quality-controlled in situ data and its role in quantifying the global water cycle. *Theor. Appl. Climatol.*, **115**, 15–40, https://doi.org/10.1007/s00704-013-0860-x.

Si, D., and Y. Ding, 2016: Oceanic forcings of the interdecadal variability in East Asian summer rainfall. *J. Climate*, **29**, 7633–7649, https://doi.org/10.1175/JCLI-D-15-0792.1.

——, ——, and Y. Liu, 2009: Decadal northward shift of the Meiyu belt and the possible cause. *Chin. Sci. Bull.*, **54**, 4742–4748, https://doi.org/10.1007/s11434-009-0385-y.

Smith, T. M., and R. W. Reynolds, 2003: Extended reconstruction of global sea surface temperatures based on COADS data (1854–1997). *J. Climate*, **16**, 1495–1510, https://doi.org/10.1175/1520-0442-16.10.1495.

Sun, J., H. Wang, and W. Yuan, 2009: Role of the tropical Atlantic sea surface temperature in the decadal change of the summer North Atlantic Oscillation. *J. Geophys. Res.*, **114**, D20110, https://doi.org/10.1029/2009JD012395.

Takaya, K., and H. Nakamura, 2001: A formulation of a phase-independent wave-activity flux for stationary and migratory quasigeostrophic eddies on a zonally varying basic flow. *J. Atmos. Sci.*, **58**, 608–627, https://doi.org/10.1175/1520-0469(2001)058<0608:AFOAPI>2.0.CO;2.

Tao, W., G. Huang, K. Hu, X. Qu, G. Wen, and Y. Gong, 2014: Different influences of two types of El Niños on the Indian Ocean SST variations. *Theor. Appl. Climatol.*, **117**, 475–484, https://doi.org/10.1007/s00704-013-1022-x.

——, ——, R. Wu, K. Hu, P. Wang, and D. Chen, 2017: Asymmetry in summertime atmospheric circulation anomalies over the northwest Pacific during decaying phase of El Niño and La Niña. *Climate Dyn.*, **49**, 2007–2023, https://doi.org/10.1007/s00382-016-3432-9.

Ting, W., S. He, Q. Yan, W. Dong, and X. Wen, 2018: Decadal shift in west China autumn precipitation and its association with sea surface temperature. *J. Geophys. Res. Atmos.*, **123**, 835–847, https://doi.org/10.1002/2017JD027092.

Wang, L., P. Xu, W. Chen, and Y. Liu, 2017: Interdecadal variations of the Silk Road pattern. *J. Climate*, **30**, 9915–9932, https://doi.org/10.1175/JCLI-D-17-0340.1.

——, G. Huang, W. Chen, W. Zhou, and W. Wang, 2018: Wet-to-dry shift over Southwest China in 1994 tied to the warming of tropical warm pool. *Climate Dyn.*, **51**, 3111–3123, https://doi.org/10.1007/s00382-018-4068-8.

Watanabe, M., and F. Jin, 2002: Role of Indian Ocean warming in the development of Philippine Sea anticyclone during ENSO. *Geophys. Res. Lett.*, **29**, 1478, https://doi.org/10.1029/2001GL014318.

Weng, H., K. M. Lau, and Y. Xue, 1999: Multi-scale summer rainfall variability over China and its long-term link to global sea surface temperature variability. *J. Meteor. Soc. Japan*, **77**, 845–857, https://doi.org/10.2151/jmsj1965.77.4_845.

Wu, B., J. Lin, and T. Zhou, 2016: Interdecadal circumglobal teleconnection pattern during boreal summer. *Atmos. Sci. Lett.*, **17**, 446–452, https://doi.org/10.1002/asl.677.

Wu, R., Z. Wen, S. Yang, and Y. Li, 2010: An interdecadal change in southern China summer rainfall around 1992/93. *J. Climate*, **23**, 2389–2403, https://doi.org/10.1175/2009JCLI3336.1.

Xie, S.-P., K. Hu, J. Hafner, H. Tokinaga, Y. Du, G. Huang, and T. Sampe, 2009: Indian Ocean capacitor effect on Indo-western Pacific climate during the summer following El Niño. *J. Climate*, **22**, 730–747, https://doi.org/10.1175/2008JCLI2544.1.

Xing, Y., and R. H. Ree, 2017: Uplift-driven diversification in the Hengduan Mountains, a temperate biodiversity hotspot. *Proc. Natl. Acad. Sci. USA*, **114**, E3444–E3451, https://doi.org/10.1073/pnas.1616063114.

Xu, Z., K. Fan, and H. Wang, 2015: Decadal variation of summer precipitation over China and associated atmospheric circulation after the late 1990s. *J. Climate*, **28**, 4086–4106, https://doi.org/10.1175/JCLI-D-14-00464.1.

Yanai, M., S. Esbensen, and J.-H. Chu, 1973: Determination of bulk properties of tropical cloud clusters from large-scale heat and moisture budgets. *J. Atmos. Sci.*, **30**, 611–627, https://doi.org/10.1175/1520-0469(1973)030<0611:DOBPOT>2.0.CO;2.

Yang, Q., Z. Ma, X. Fan, Z.-L. Yang, Z. Xu, and P. Wu, 2017: Decadal modulation of precipitation patterns over eastern China by sea surface temperature anomalies. *J. Climate*, **30**, 7017–7033, https://doi.org/10.1175/JCLI-D-16-0793.1.

Yao, C., S. Yang, W. Qian, Z. Lin, and M. Wen, 2008: Regional summer precipitation events in Asia and their changes in the past decades. *J. Geophys. Res.*, **113**, D17107, https://doi.org/10.1029/2007JD009603.

Yao, S.-L., G. Huang, R.-G. Wu, X. Qu, and D. Chen, 2016: Inhomogeneous warming of the tropical Indian Ocean in the CMIP5 model simulations during 1900–2005 and associated mechanisms. *Climate Dyn.*, **46**, 619–636, https://doi.org/10.1007/s00382-015-2602-5.

——, J.-J. Luo, G. Huang, and P. Wang, 2017: Distinct global warming rates tied to multiple ocean surface temperature changes. *Nat. Climate Change*, **7**, 486–491, https://doi.org/10.1038/nclimate3304.

Yonetani, T., and G. J. J. McCabe, 1994: Abrupt changes in regional temperature in the conterminous United States, 1895–1989. *Climate Res.*, **4**, 13–23, https://doi.org/10.3354/cr004013.

Yu, L., T. Furevik, O. H. Otterå, and Y. Gao, 2015: Modulation of the Pacific Decadal Oscillation on the summer precipitation over East China: A comparison of observations to 600-years

control run of Bergen Climate Model. *Climate Dyn.*, **44**, 475–494, https://doi.org/10.1007/s00382-014-2141-5.

Zhang, K., S. Pan, L. Cao, Y. Wang, Y. Zhao, and W. Zhang, 2014: Spatial distribution and temporal trends in precipitation extremes over the Hengduan Mountains region, China, from 1961 to 2012. *Quat. Int.*, **349**, 346–356, https://doi.org/10.1016/j.quaint.2014.04.050.

Zhang, P., G. Li, X. Fu, Y. Liu, and L. Li, 2014: Clustering of Tibetan Plateau vortices by 10–30-day intraseasonal oscillation. *Mon. Wea. Rev.*, **142**, 290–300, https://doi.org/10.1175/MWR-D-13-00137.1.

Zhang, T., B. Li, Y. He, J. Du, H. Niu, and H. Xin, 2015: Spatial and temporal distribution of precipitation based on corrected TRMM data in Hengduan Mountains (in Chinese). *Ziran Ziyuan Xuebao*, **30**, 260–270.

Zhou, T., D. Gong, J. Li, and B. Li, 2009: Detecting and understanding the multi-decadal variability of the East Asian summer monsoon—Recent progress and state of affairs. *Meteor. Z.*, **18**, 455–467, https://doi.org/10.1127/0941-2948/2009/0396.

Zhu, G., T. Pu, T. Zhang, H. Liu, X. Zhang, and F. Liang, 2013: The accuracy of TRMM precipitation data in Hengduan Mountainous Region, China (in Chinese). *Dili Kexue*, **33**, 1125–1131.

——, and Coauthors, 2016: Variation of Thornthwaite moisture index in Hengduan Mountains, China. *Chin. Geogr. Sci.*, **26**, 687–702, https://doi.org/10.1007/s11769-016-0820-3.